electronics

MDPI

Article

High-Gain Planar Array of Reactively Loaded Antennas for Limited Scan Range Applications

Ronis Maximidis [1,*], Diego Caratelli [1,2], Giovanni Toso [3] and A. Bart Smolders [1]

1 Department of Electrical Engineering, Electromagnetics Group, Eindhoven University of Technology, 5600 MB Eindhoven, The Netherlands; diego.caratelli@antennacompany.com (D.C.); A.B.Smolders@tue.nl (A.B.S.)
2 Department of Research and Development, The Antenna Company, 5656 AE Eindhoven, The Netherlands
3 Antenna and Sub-Millimeter Waves Section, European Space Agency, ESA/ESTEC, 2200 AG Noordwijk, The Netherlands; giovanni.toso@esa.int
* Correspondence: R.T.Maximidis@tue.nl; Tel.: +31-40-247-2647

Received: 15 July 2020; Accepted: 18 August 2020; Published: 25 August 2020

check for updates

Abstract: This paper proposes a novel high-gain antenna element that can be used in antenna arrays that only require a limited scan range. Each high-gain antenna element uses a linear sub-array of highly-coupled open-ended waveguides. The active central element of this sub-array is directly fed, while the remaining passive waveguides are reactively loaded. The loads are implemented by short-circuits positioned at various distances from the radiating aperture. The short-circuit positions control the radiation pattern properties and the scattering parameters of the array. The proposed sub-array antenna element is optimized in the presence of the adjacent elements and provides a high gain and a flat-top main lobe. The horizontal distance between the sub-array centers is large in terms of wavelengths, which leads to limited scanning capabilities in the E-plane. However, along the vertical axis, the element spacing is around 0.6 wavelength at the central frequency that is beneficial to achieve a wider scan range in the H-plane. We show that the sub-array radiation pattern sufficiently filters the grating lobes which appear in the array factor along the E-plane. To demonstrate the performance of the proposed array configuration, an array operating at 28.0 GHz is designed. The designed array supports scan angles up to ±7.5° along the E-plane and ±24.2° along the H-plane

Keywords: phased arrays; high-gain array element; sub-array; mm-wave; flat-top pattern

1. Introduction

To support the growing demand for high data rates, the telecommunication industry is constantly moving to higher frequencies where larger operational bandwidths are available [1]. However, the propagation loss of radio-wave signals also increases significantly at millimeter-wave frequencies, thus severely limiting the communication range. One way to deal with the increased path losses is to compensate them by increasing the directivity using antenna arrays with electronic beamforming [2,3]. An alternative solution consists in the use of multibeam antennas which reduce the overall system footprint and can enhance, significantly, the system capacity [4]. However, the cost of electronic components required for the development of such a complex antenna system increases dramatically as the frequency of operation becomes higher. Therefore, only small-size antenna arrays with moderate directivities have been developed until now.

On the other hand, there are plenty of applications that require a very high antenna gain but only over a limited field of view (FoV). Examples in this respect are given by point-to-point or point-to-multipoint backhaul links and antennas for sub-urban coverage. For such applications, one can use array elements characterized by a large aperture and, therefore, high directivity [5].

This allows reducing the number of radiating elements needed to achieve the required gain levels. In turn, this translates into reduced design complexity and manufacturing costs of the feeding network. However, the use of radiating elements with large apertures leads to the appearance of grating lobes in the visible region. The distance between the main lobe and the grating lobes is inversely proportional to the distance between sub-array centers. Therefore, the inter-element spacing should be selected in such a way to keep the grating lobes outside the field of view for all scan angles. To this end, the aperture size should be restricted to certain dimensions. A useful design approach to overcome this drawback, and which is implemented in this research study, is based on the use of overlapping radiating apertures, i.e., the use of the same aperture for multiple feed points. In this way, we can achieve the required levels of gain while maintaining the overall array compactness. Even though overlapping techniques allow keeping grating lobes outside the FoV, the presence of grating lobes still has, per se, certain adverse effects on the side-lobe characteristics of the overall array. More specifically, in transmit mode, they can result in energy leakage along undesired directions that, in turn, can cause a waste of power and potential electromagnetic interferences. In the receive mode, grating lobes can cause the reception of spurious radio signals from undesired directions and, thereby, a degradation of the signal-to-interference ratio. Therefore, appropriate measures have to be taken so as to minimize the detrimental impact of grating lobes. The solution, adopted in this paper, is to filter the grating lobes by the proper shaping of the embedded radiation pattern featured by the individual array element [5,6].

A number of techniques have been developed to reduce the distance between radiating apertures. One can use a complex feeding network to distribute the energy of a port to multiple radiating apertures, enlarging, in this way, the size of each radiating element. Nonetheless, the feeding network becomes very complex even for a small number of array elements; therefore, this technique has found limited applications, mostly in space [7,8]. Another approach consists in using partially reflective surfaces placed above the array structure [9–11]. However, the reflective surfaces increase the height of the structure and reduce its mechanical robustness.

In our previous work [6], we proposed a technique to reduce the separation between the phase centers of a one-dimensional array so as to avoid the use of complex overlapping networks or reflective surfaces. In the proposed design approach, each radiating aperture consists of a linear sub-array composed of one directly fed open-ended waveguide radiator and a large number of short-circuited highly-coupled waveguide elements. The energy is delivered to the passive waveguides by free-space coupling and the sub-array structure is designed in such a way to deliver energy to the passive elements of the adjacent sub-arrays as well. As a result, an effective overlapping between sub-arrays can be realized without the use of any additional power distribution network. The positions of the short circuits define the impedance experienced by the electromagnetic field coupled to the passive waveguides. Due to the low loss of the waveguides, said impedance is mainly reactive. Therefore, by optimizing the positions of short circuits, we can control the wave radiation process by the individual passive waveguide and, in this way, shape the embedded sub-array radiation pattern as well as control the active scattering parameters of the overall array structure.

In the present research study, we apply the technique proposed in [6] to the design of a planar antenna array composed of linear sub-arrays. The embedded radiation pattern of the realized antenna sub-array provides a limited scan range along the sub-array main axis (E-plane) but a substantially larger coverage along the orthogonal axis (H-plane). The array presented in this paper operates at Ka-band at 28.0 GHz, where several emerging wireless applications are being developed [12] but can be easily scaled to any desired frequency.

This paper presents the following new scientific contributions:

- Extension of the overlapping technique based on free-space coupling to design a planar array. The optimized array features high gain and requires a much smaller number of active elements as compared to traditional phased-array systems.
- A theoretical framework to optimize and analyze the proposed class of arrays for any specific application.

The paper is organized as follows. In Section 2, we describe the design procedure, and introduce the mathematical model used for the array optimization; the interested reader can find a more detailed derivation of the model in [6]. In Section 3.1, we present an overlapping sub-array structure featuring an embedded flat-top radiation pattern. Next, in Section 3.2 we use the designed subarray as a building block for the development of a high-gain antenna array. The paper closes with the main conclusions and future directions.

2. Method

Figure 1 shows a schematic of a reactively loaded antenna array consisting of N_a directly-fed waveguides and N_p reactively loaded waveguides. The employed design procedure is general; therefore, the active and passive elements can be randomly distributed across the array.

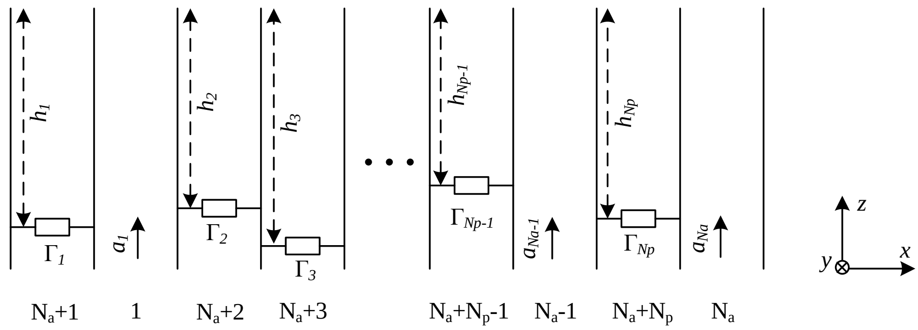

Figure 1. Schematic view of a reactively loaded waveguide antenna array.

The total electric field $\vec{E}(\theta,\varphi)$ radiated by such a structure is given from [6]:

$$\vec{E}(\theta,\varphi) = \mathbf{a}^T \cdot \left[\vec{\mathbf{E}}_a(\theta,\varphi) + \underline{\mathbf{S}}_c \cdot \left(\left[\left(\underline{\boldsymbol{\Gamma}}_p \cdot e^{-2\underline{\boldsymbol{\gamma}}_p \cdot \underline{\mathbf{h}}_p} \right)^{-1} - \underline{\mathbf{S}}_p \right]^{-1} \right)^T \cdot \vec{\mathbf{E}}_p(\theta,\varphi) \right] \tag{1}$$

with the superscript ^{T} denoting the matrix transposition; the subscripts a and p refer to active and passive elements, respectively. Besides, θ and φ are the conventional spherical angles.

In Equation (1), the vector $\mathbf{a}$ contains the excitation coefficients of the directly-fed array elements, and $\vec{\mathbf{E}}_a(\theta,\varphi)$, $\vec{\mathbf{E}}_p(\theta,\varphi)$ are the vectors containing the electromagnetic field contributions radiated by the active and passive elements, respectively. The matrices $\underline{\mathbf{S}}_p$ and $\underline{\mathbf{S}}_c$ are blocks of the scattering matrix $\underline{\mathbf{S}}$, they are relevant to the entire structure and describe the interaction between the passive waveguides and the coupling between the passive and directly fed waveguides, respectively. Finally, $\underline{\boldsymbol{\Gamma}}_p$, $\underline{\boldsymbol{\gamma}}_p$, and $\underline{\mathbf{h}}_p$ are diagonal matrices containing the reflection coefficient of the load, the complex propagation constant, and the length of the passive waveguides, respectively.

In [6], it has been demonstrated that the scattering matrix of the active elements can be calculated as follows:

$$\underline{\mathbf{S}}'_a = \underline{\mathbf{S}}_a + \underline{\mathbf{S}}_c \cdot \left[\left(\underline{\boldsymbol{\Gamma}}_p \cdot e^{-2\underline{\boldsymbol{\gamma}}_p \cdot \underline{\mathbf{h}}_p} \right)^{-1} - \underline{\mathbf{S}}_p \right]^{-1} \cdot \underline{\mathbf{S}}_c^T \tag{2}$$

where $\underline{\mathbf{S}}_a$ is the block matrix of $\underline{\mathbf{S}}$ describing the interaction between active elements.

On the basis Equations (1) and (2), the design of the proposed type of arrays can be performed using the following procedure:

1. Decide on the array topology and the minimum number of sub-arrays N_S useful to approximate a large array environment for the central sub-array.
2. Decide on the number of elements per sub-array, N_E.
3. Obtain the scattering matrix and the embedded element patterns for all the elements of the $(N_S \times N_E) \times (N_S \times N_E)$ array.

4. Choose an optimization algorithm and select the optimization parameters.
5. Define the objective function on the basis of Equaitons (1) and (2).
6. After optimization, increase the array size by adding sub-arrays until there is no change in the embedded radiation pattern of the central sub-array.
7. Use the obtained pattern as the embedded element pattern for the design of arrays of any size.

As it is apparent from Equations (1) and (2), the main optimization parameters are ($\underline{\mathbf{\Gamma}}_p$, $\underline{\boldsymbol{\gamma}}_p$, $\underline{\mathbf{h}}_p$), which define the electrical length of the passive waveguides and their loading profile. The proposed design procedure has been implemented in Matlab [13].

3. Design

3.1. Sub-Array Design

In this paper, we design a planar array built up from linear sub-arrays. The sub-arrays have to support a wide scan range in the H-plane with a reduced scanning capability in the E-plane. The design starts from the structure of Figure 2a, where a linear antenna sub-array of N_E = 13 open-ended waveguides is placed in an $N_A = 9 \times 3$ array configuration.

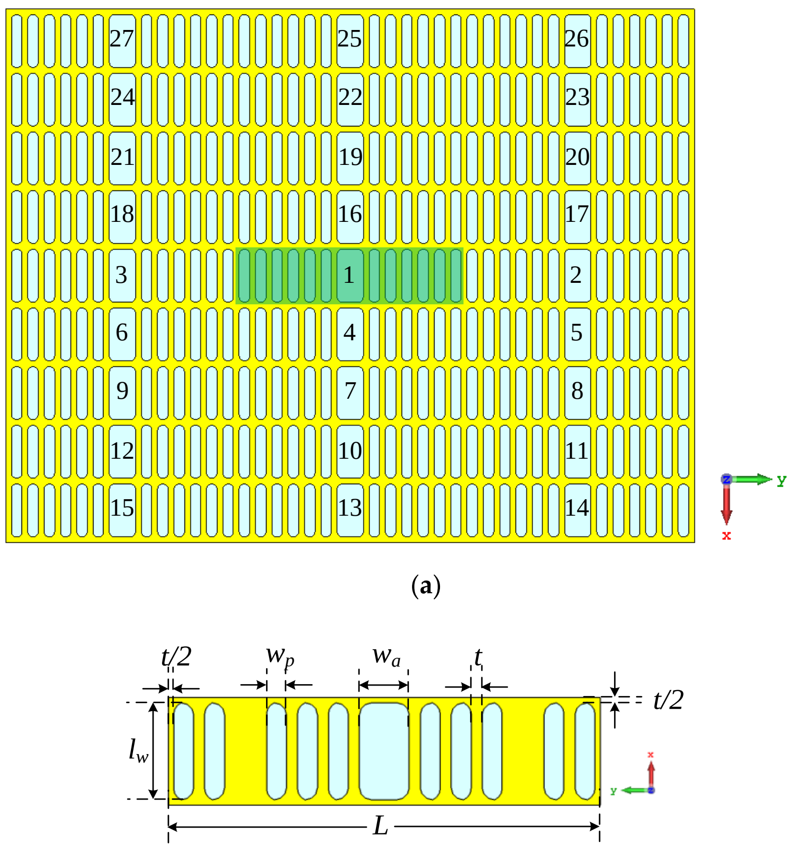

(**a**)

(**b**)

Figure 2. (**a**) Planar $N_A = 9 \times 3$ array configuration using high-gain sub-arrays of open-ended waveguides. The central sub-array is highlighted in green, whereas the relevant geometrical parameters are reported in (**b**).

The length of the sub-array, L = 2.653λ_0, with λ_0 denoting the free-space wavelength, was chosen in such a way as to achieve a FoV of about ±8°. The choice of the length, $l_w = 0.6\lambda_0$, of the waveguides is governed by the cut-off condition of the fundamental TE_{01} mode, that is $l_w > 0.5\lambda_0$. The width of the passive waveguides, $w_p = 0.12\lambda_0$, the thickness of the walls, $t = 0.0679\lambda_0$, as well as the relevant rounding radius of 0.8 mm were chosen so as to simplify the manufacturing process. Finally, the width of the central waveguide, $w_a = 0.3\lambda_0$, is optimized in a way to achieve good impedance matching characteristics. At the initial design step, the length of all the waveguides is set to $0.1\lambda_g$, where λ_g denotes the guided wavelength of the fundamental TE_{01} mode of the passive waveguides. At the working frequency, f_0 = 28.0 GHz, and for the specified waveguide dimensions, we get λ_g = 21.104 mm.

In a linear array, the angular position of the grating lobes is a function of the separation d between antenna elements and the scan angle θ_0, and is given by:

$$\sin\theta_p = \sin\theta_0 + \frac{p\lambda_0}{d} \tag{3}$$

where $p = \pm 1, \pm 2, \ldots$ is chosen in such a way as to define an angle with real value, as per the condition $|\sin\theta_p| \leq 1$. The maximum scan angle of the array factor before the appearance of the first grating lobe in the field of view is $\theta_p = -\theta_0$.

Using Equation (3), we can evaluate the maximum theoretical scan range in the two main planes of the array of sub-arrays in Figure 2, which is ±10.86° along the E-plane and ±48.47° along the H-plane. Therefore, theoretically, in order to maximize the gain flatness and minimize the radiation to the undesired directions, the sub-array embedded radiation pattern has to have a high gain flat-top shape in the calculated scan range and should have a low gain outside this range. However, a radiation pattern with such a jump discontinuity in the relevant gain distribution cannot be synthesized using a limited-size array, unless we introduce a transition region which, however, reduces the maximum scan range.

Therefore, on the basis of this observation, the flat-top region has been set to ±8.0° and ±40.0° along the E-plane and the H-plane, respectively. Additional design goals are enforced so as to achieve maximal directivity along the boresight, low side-lobe levels (SLL < −15 dB) along the E-plane, and high return loss combined with low coupling coefficients at the active ports of the array at the central operating frequency. Equation (4) shows the objective function used for the optimization:

$$\begin{aligned}\Psi_O\big(f_0,\mathbf{h}_p\big) = &\sum_{j=1}^{N_a}\Big|S'_{1j,a}\big(f_0,\mathbf{h}_p\big)\Big| - D(f_0,\mathbf{h}_p,\theta_0,0^\circ) + \left|\int_0^{\theta_h}\Big[D(f_0,\mathbf{h}_p,\theta,0^\circ) - D(f_0,\mathbf{h}_p,\theta_0,0^\circ)\Big]d\theta\right| \\ &+ \left|\int_0^{\theta_e}\Big[D(f_0,\mathbf{h}_p,\theta,90^\circ) - D(f_0,\mathbf{h}_p,\theta_0,90^\circ)\Big]d\theta\right| - 10\Bigg\{\Big|D(f_0,\mathbf{h}_p,\theta_c,90^\circ) - D(f_0,\mathbf{h}_p,\theta_0,90^\circ)\Big| \\ &- \min_{\theta\in[\theta_{SL},90^\circ]}\frac{D(f_0,\mathbf{h}_p,\theta_e,90^\circ)}{D(f_0,\mathbf{h}_p,\theta,90^\circ)}\Bigg\},\end{aligned} \tag{4}$$

where the first term is to minimize $S'_{1j,a}$, $j = 1,2, \ldots, N_a$, and, in this way, optimize the scattering parameters of the central sub-array. The second term maximizes the broadside directivity. The next two terms are introduced to maximize the flat-top regions, with θ_h = 40° and θ_e = 8°, along the H-plane and E-plane, respectively. Finally, the last two terms are useful to minimize the directivity outside the field of view along the E-plane, the relative directivity at the critical angle θ_c = 14°, and the SLL for $\theta \in [\theta_{SL}, 90°]$ with θ_{SL} = 20°. The designed sub-array is symmetrical with boresight radiation pattern characteristics along the z-axis. Therefore, we can confine the optimization process to the angular range $\varphi \in [\theta_{SL}, 90°]$. Figure 3 shows graphically the defined angular regions.

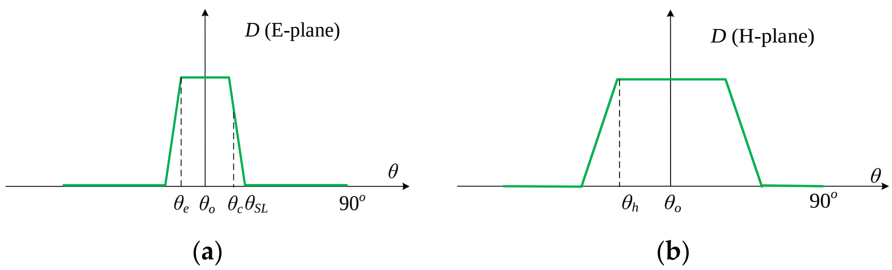

Figure 3. Graphical representation of the array radiation pattern mask along the (**a**) E-plane and (**b**) H-plane.

Utilizing the objective function defined in Equation (4), the design procedure is turned into the solution of the following minimization problem:

$$\underset{0 \leq \underline{\mathbf{h}}_p \leq 0.5\lambda_g}{\operatorname{argmin}} \; \Psi_O\left(f_0, \underline{\mathbf{h}}_p\right) \tag{5}$$

Due to the symmetry of the considered sub-array structure, the number of design parameters is equal to half the number of passive waveguides embedded in each individual sub-array.

The optimization procedure starts with the calculation of the embedded element patterns and scattering matrix of an array of 9 × (3 × 13) elements. To this end, a suitable full-wave electromagnetic solver is used [14]. The obtained results are then imported into an in-house developed dedicated software that implements the proposed design procedure. Next, using Equations (1) and (2), the objective function of Equation (4) is implemented. Then, the Global Search Optimization routine embedded in Matlab [13] is adopted to address the minimization problem described by Equation (5). The Global Search Optimization technique combines a global pattern-search-based optimizer with a local gradient-based optimization algorithm. Details of the Global Search Optimization algorithm can be found in [15].

The optimal positions of the short-circuits along the passive waveguides are listed in Table 1, where the waveguides have been numbered starting from the closest one to the central active element. A cross-section of the resulting array is shown in Figure 4.

Table 1. Passive waveguides lengths of the optimized structure.

Section Length	h1	h2	h3	h4	h5	h6
Value in λg	0.196	0.205	0.193	0.0000	0.098	0.206

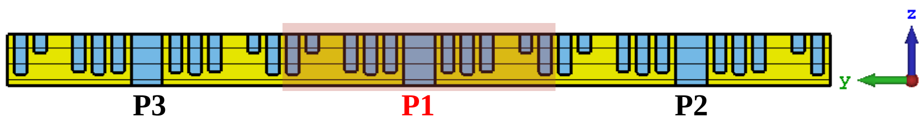

Figure 4. Cross-section of three sub-arrays along the sub-array main axis. The waveguides are shown in blue.

The electromagnetic characteristics of the designed sub-array structure have been successfully validated by using a full-wave solver [14]. After the optimization procedure, the number of sub-arrays has been gradually increased until the radiation pattern of the central sub-array does not change significantly any longer. Figure 5 shows the three main cuts of the embedded radiation pattern of the central sub-array when integrated in 9 × 3, 11 × 5, and 15 × 9 array configurations.

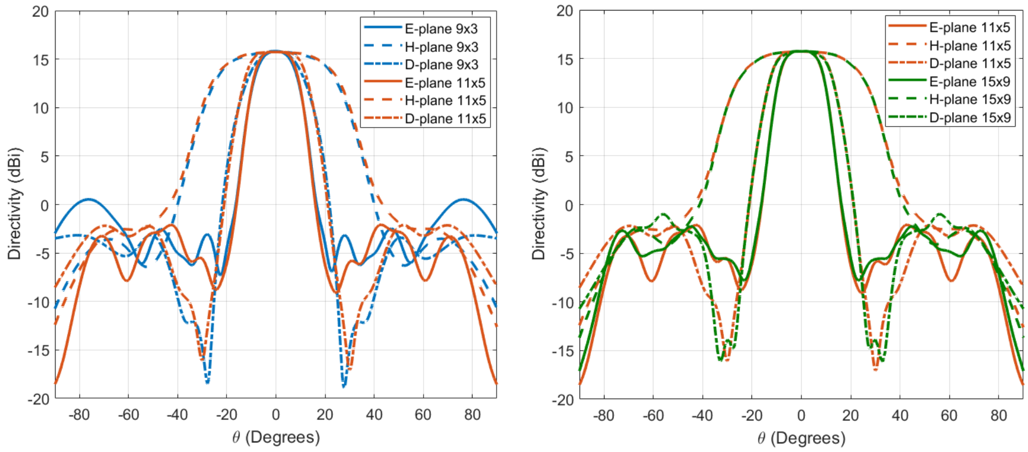

(**a**) (**b**)

Figure 5. Embedded element pattern comparison of the central subarrays: (**a**) 9 × 3 and 11 × 5; (**b**) 11 × 5 and 15 × 9 at the design frequency f_0 = 28.0 GHz.

In Figure 5, one can notice a non-negligible change in the embedded radiation patterns along the E- and D-planes when the array size is increased from 9 × 3 to 11 × 5 sub-array elements. More specifically, even though the half-power beam-width does not vary along the H-plane, it differs significantly along the other planes, by 0.3° along the E-plane and by 1.3° along the D-plane. Furthermore, a large deviation of about 7.8 dB is observed in the sidelobe level along the E-plane. No meaningful performance variations occur for further increases of the array size, i.e., to 15 × 9 elements. As a matter of fact, the maximal difference inside the half-power beam-width along the various planes is about 0.1 dB, whereas the deviation in terms of the sidelobe level is negligible. An additional investigation has been performed on the active reflection coefficient of the central sub-array element in the 9 × 3, 11 × 5, and 15 × 9 array topologies. As it appears in Figure 6, the active reflection coefficients featured by the central elements of the 11 × 5 and 15 × 9 arrays show rather similar behavior but differ quite significantly from the one obtained for the 9 × 3 array. On the basis of the reported results, the radiation pattern of the central element of the 11 × 5 array has been selected as the embedded sub-array pattern, whose main parameters are detailed in Table 2.

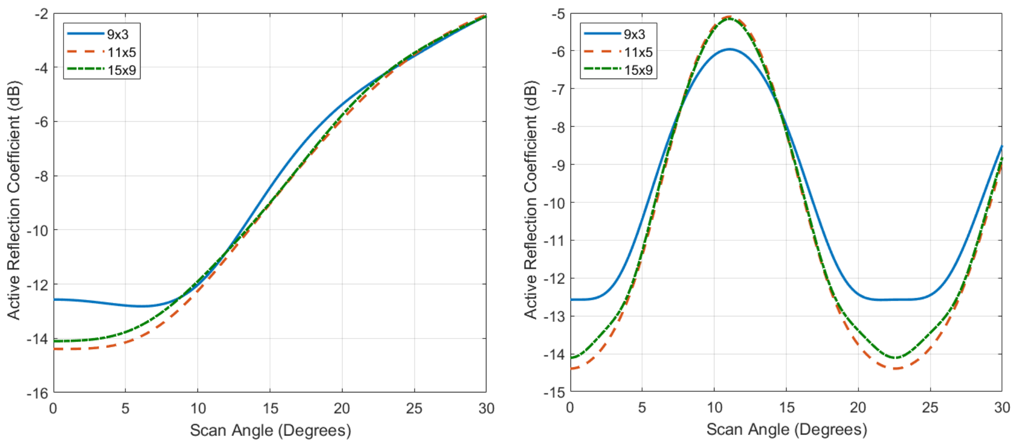

(**a**) (**b**)

Figure 6. Active reflection coefficient versus scan angle θ_0 of the central element for (**a**) φ = 0° and (**b**) φ = 90° at the design frequency f_0 = 28.0 GHz.

Table 2. Embedded radiation pattern characteristics of the 11 × 5 array.

Cuts	D(0°) (dBi)	BW(−3 dB) (°)	BW(−0.5 dB) (°)	SLL (dB)
H-plane	15.7	±25.7	±14.9	−18.2
E-plane	15.7	±9.3	±5.9	−17.8
D-plane	15.7	±12.9	±8.5	−17.8

From Figure 5b and Table 2, it can be concluded that the scan range along the E-plane is close to the optimization objective, whereas a gap is observed in relation to the scan range along the H-plane. The sub-array directivity for $\theta_0 = 0°$ is 15.7 dBi, which is 2.3 dB higher than the nominal directivity calculated on the basis of the physical aperture area A_{ap} of the individual sub-array, that is:

$$D_{ap} = \frac{4\pi}{\lambda_0^2} A_{ap} = 13.4 \text{ dBi} \quad (6)$$

We can conclude that the sub-array directivity has been enhanced thanks to the overlapping with adjacent sub-arrays. This increase in directivity can be translated in a 41% reduction of the required transmit power or, equivalently, a 23% reduction in the number of required sub-arrays. In order to provide an insight into the process that is responsible for the enhancement of the directivity, the electric field distribution over the radiating aperture of the 11 × 5 array is reported in Figure 7 when only the central sub-array is active and the other sub-arrays are terminated on matched loads.

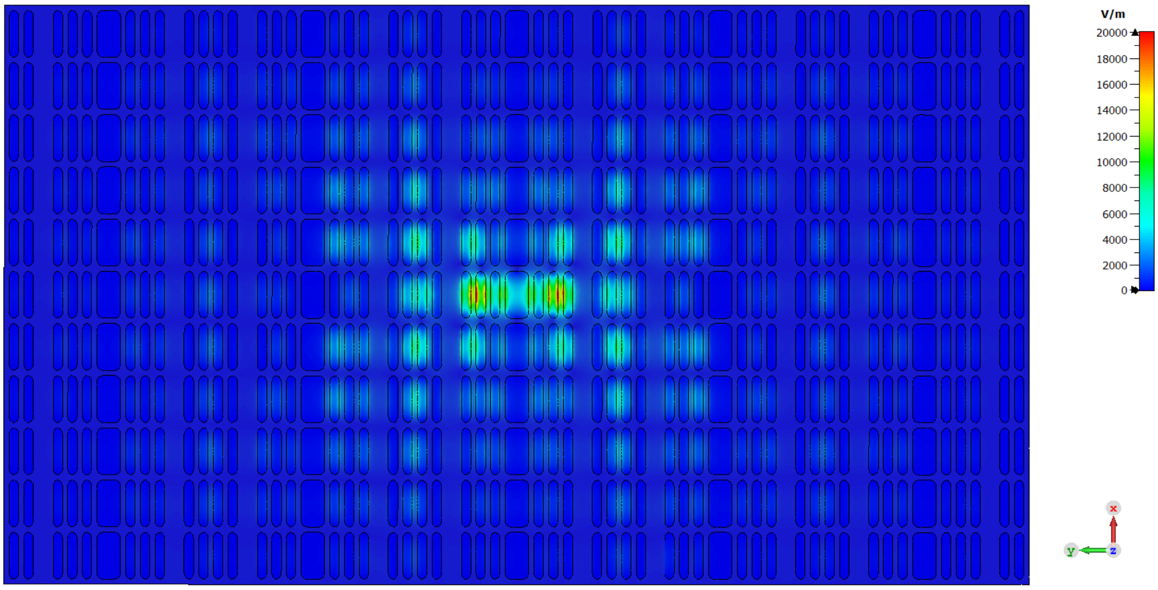

Figure 7. Calculated electric field distribution of the central sub-array when all other sub-arrays are matched in the 11 × 5 array at the design frequency f_0 = 28.0 GHz.

From Figure 7, it can be seen that the electric field propagates in a very effective way towards adjacent sub-arrays virtually in all directions. Effectively, all the sub-arrays contribute, to some extent, to the electromagnetic field radiation process. This mechanism enables the sub-array overlapping and, from there, the mentioned directivity enhancement and capability of synthesizing complex-shaped radiation pattern. It should be noted however that, while propagating, the electromagnetic field gradually decays and eventually displays a limited intensity along the edge elements of the array. This is the reason why a further increase in the number of sub-arrays (beyond the size of 11 × 5) does not significantly affect the central sub-array characteristics.In Figure 8, the embedded radiation pattern of the central sub-array of the 11 × 5 element array is presented in the uv-plane, where u = sinθcosφ and v = sinθsinφ.

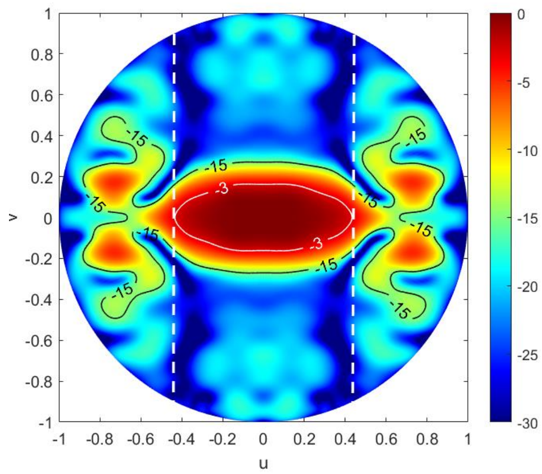

Figure 8. Embedded element pattern of the optimized sub-array at the center of the 11 × 5 array, displayed in the uv-plane, where u = sinθcosφ and v = sinθsinφ. The black and white solid lines encircle areas with a level higher than −15 dB and −3 dB compared to the maximum value. All presented results are obtained at the design frequency f_0 = 28.0 GHz.

Figure 8 shows that the areas where the SLL is larger than −15 dB are outside the region defined by the vertical dotted lines. This region identifies the angular sector where the grating lobes would occur assuming that the considered sub-array is used in a uniform planar array configuration. The performance of such an array can be estimated by analyzing the embedded sub-array pattern presented in Figure 8. Along the H-plane, the grating lobes are outside the visible region over the entire scan range. However, along the E-plane, the grating lobes are inside the visible region. In order to achieve a 10 dB grating-lobe rejection level, we have to limit the scan range to ±8.7°. On the other hand, if a 15 dB grating-lobe rejection level is enforced, the scan range shrinks further to ±6.5°.

The active voltage standing wave ratio (VSWR) versus frequency and scan angle of the central sub-array of the 11 × 5 array configuration is shown in Figure 9.

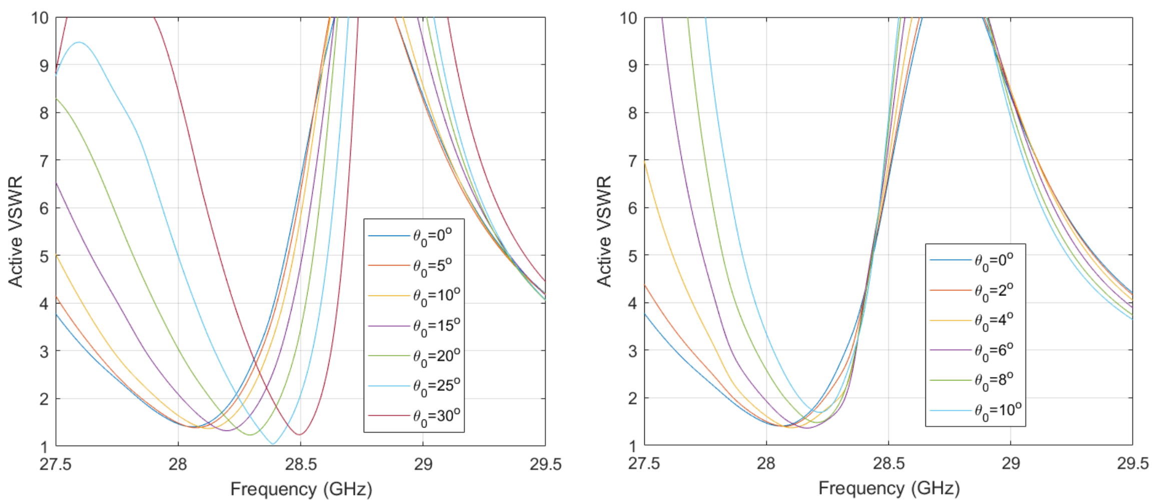

(**a**) (**b**)

Figure 9. Active voltage standing wave ratio (VSWR) versus frequency and scan angle for (**a**) H-plane and (**b**) E-plane of the central sub-array of the 11 × 5 array.

Figure 9 shows that the designed sub-array is intrinsically matched, though the relevant impedance matching band shifts with the scan angle. The maximum scanning range can be obtained on the basis of application-specific requirements for active VSWR and bandwidth. In case, where broadband behavior is needed, the integration of a suitable impedance matching network can be explored. The design of such a matching network is outside the scope of this work.

3.2. Array Design

In this section, we use the designed sub-array to realize an antenna array that features a rotationally symmetric mainbeam with a high directivity level of at least 46 dBi. To achieve these goals, a planar array of 65×19 elements is required. The simplest approach to the design of such an array would be to adopt the same embedded radiation pattern of the central sub-array analyzed in the previous section for all the array elements. However, this approach would not account for the fact that the edge elements experience different surroundings and, therefore, are characterized by different embedded radiation patterns. A more accurate design approach consists in the use of the embedded radiation pattern of the edge elements of the small array as an approximation of the one relevant to the edge elements of the large array, as illustrated schematically in Figure 10.

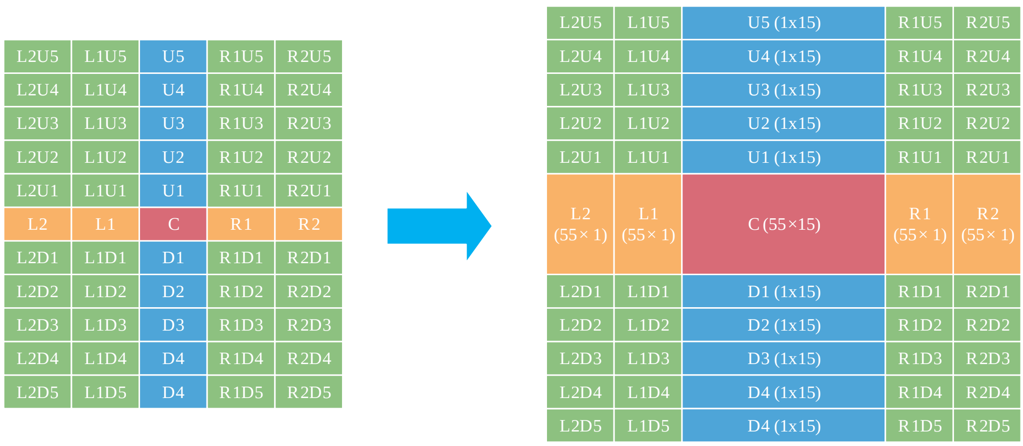

(**a**) (**b**)

Figure 10. Schematic representation of the transformation from (**a**) small array with 11×5 sub-array elements to (**b**) a large array of 65×19 elements. In (**a**) each block represents a sub-array placed in the specific location. In (**b**) the various blocks represent sub-domains (with dimensions indicated into brackets) synthesized using the relevant embedded sub-array patterns in (**a**). The green blocks are 1×1 sub-arrays.

The transformation from the 11×5 to the 65×19 array configuration is performed as follows:

1. The radiation pattern of the central element of the 11×5 array (red element in Figure 10a is used to synthesize the central 55×15 sub-array (highlighted in red in Figure 10b).
2. The elements highlighted in orange in a are used to synthesize the corresponding domains with 55×1 sub-arrays highlighted in orange in Figure 10b.
3. Similarly to step 2, the blue elements in Figure 10a are used to synthesize the domains of 1×15 sub-arrays highlighted in blue in Figure 10b.
4. Finally, the remaining green elements in Figure 10a are used as is to complete the 65×19 array in Figure 10b.

The scan characteristics along the two principal planes of the resulting 65×19 array are illustrated in Figure 11. The achieved boresight directivity level is 46.5 dBi, which is 0.1 dBi smaller than that displayed by the 65×19 array when the embedded radiation pattern of the central sub-array is used for all the elements and, therefore, the edge effect is neglected. It is worth noting, also, that the edge effect causes faster decay of the array mainbeam with the scanning angle, as it can be observed in Figure 11. In the absence of the edge effect, the array mainbeam would follow the profile of the central sub-array pattern. This non-ideality is responsible for a reduced scan range, which can be quantified as 7.5° in the E-plane, and 24.2° in the H-plane.

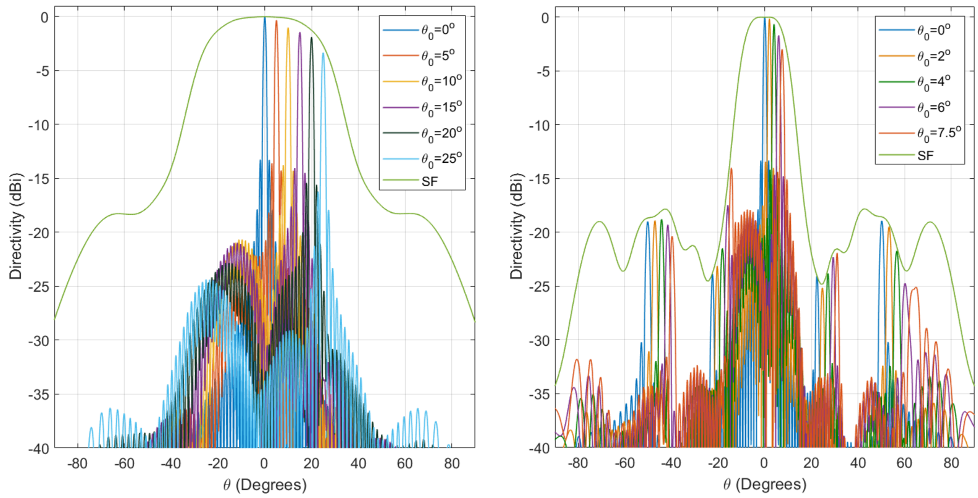

(**a**) (**b**)

Figure 11. The radiation pattern of the 65 × 19 array for various scan angles along the (**a**) H-plane and (**b**) E-plane. The figure also includes the embedded radiation pattern of the central sub-array of the 11 × 5 array, sub-array factor (SF).

To show the impact of the edge effect on the side-lobe level characteristics, the array radiation pattern evaluated using the proposed design approach for the scan angles of 25° and 7.5° along the H- and E-plane, respectively, has been compared against the corresponding one obtained when the radiation pattern of the central sub-array is used for all elements of the array; therefore, the edge effects are neglected (see Figure 12).

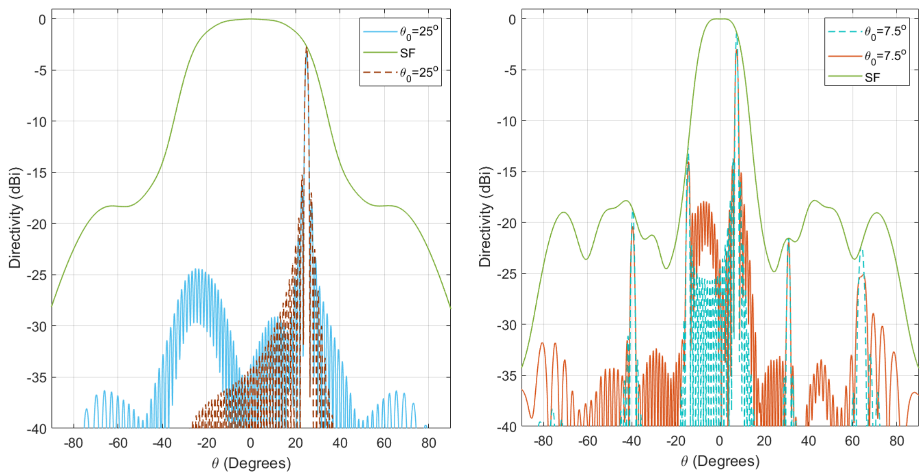

(**a**) (**b**)

Figure 12. Comparison of the radiation pattern of the 65 × 19 calculated by the proposed approach (solid line) versus an approach that assumes identical embedded radiation (dotted line) for the (**a**) H-plane and (**b**) E-plane. The figure also includes the embedded radiation pattern of the central sub-array of the 11 × 5 array (SF).

As it can be noticed in Figure 12, neglecting the edge effect leads to an overestimation of the main-beam directivity, by 0.7 dB in the H-plane, and by 1.6 dB in the E-plane, respectively. The deviation along the E-plane is more noticeable because of the smaller number, 19, of sub-arrays in that direction, as compared to the number of elements, 65, along the H-plane. Another effect of the edge elements that can be observed in Figure 12 is relevant for the increase of the sidelobe levels, by about 14.6 dB for $\theta \simeq -25.0°$ along the H-plane, and by about 7.5 dB for $\theta \simeq -7.5°$ along the E-plane. The performed comparison clearly shows the importance of including the edge effects in the analysis of the array performance.

The filtering effect of the sub-array factor for various scan angles is visualized in Figure 13e–h. For comparison, the array factor of a 65 × 19 array is presented in Figure 13a–d. Figure 13a–d shows the array factor of a 65 × 19 array for various representative scanning angles. The array elements are excited with uniform amplitude, whereas the phase tapering is optimized so to steer the array beam along the desired direction. Because of the large distance between array elements along the u-axis, grating lobes appear. On the other hand, the array element separation along the v-axis is smaller than $0.6\lambda_0$ that is instrumental in keeping the grating lobes outside the visible region, as per Equation (3), for the targeted scanning range. Figure 13e–h shows the filtering effect on the sub-array radiation pattern that is useful in the suppression of undesired grating lobes. It is worth mentioning that even though the sidelobe level of the embedded sub-array pattern is very high in some specific directions, as is shown in Figure 8, the radiation pattern of the total array has a sidelobe level below −30 dB, at the specified directions. This performance is achieved thanks to the fact that the array scanning is restricted to the angular region defined by the contour line at −3 dB level. Therefore, it has been shown that the requirement on the sub-array side lobe level can be relaxed for certain directions which are defined by the scan range of the full array. Finally, due to the uniform amplitude excitation, the side-lobe level of the total radiation pattern is about −13.27 dB. If further sidelobe level reduction is required, a suitable amplitude tapering scheme of the array excitation has to be adopted [16].

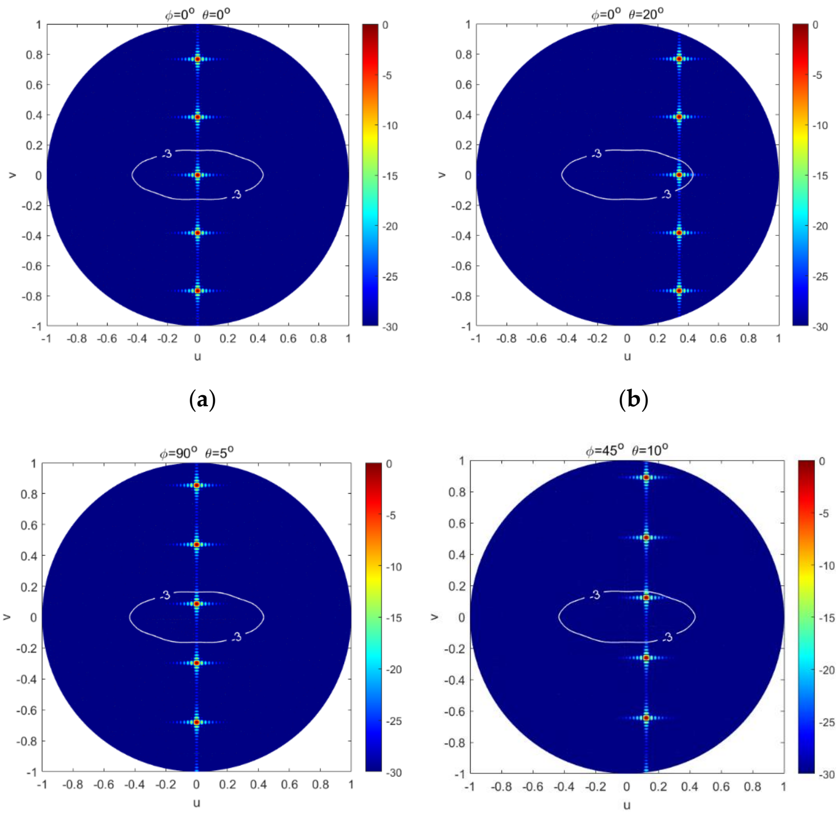

(**a**) (**b**) (**c**) (**d**)

Figure 13. *Cont.*

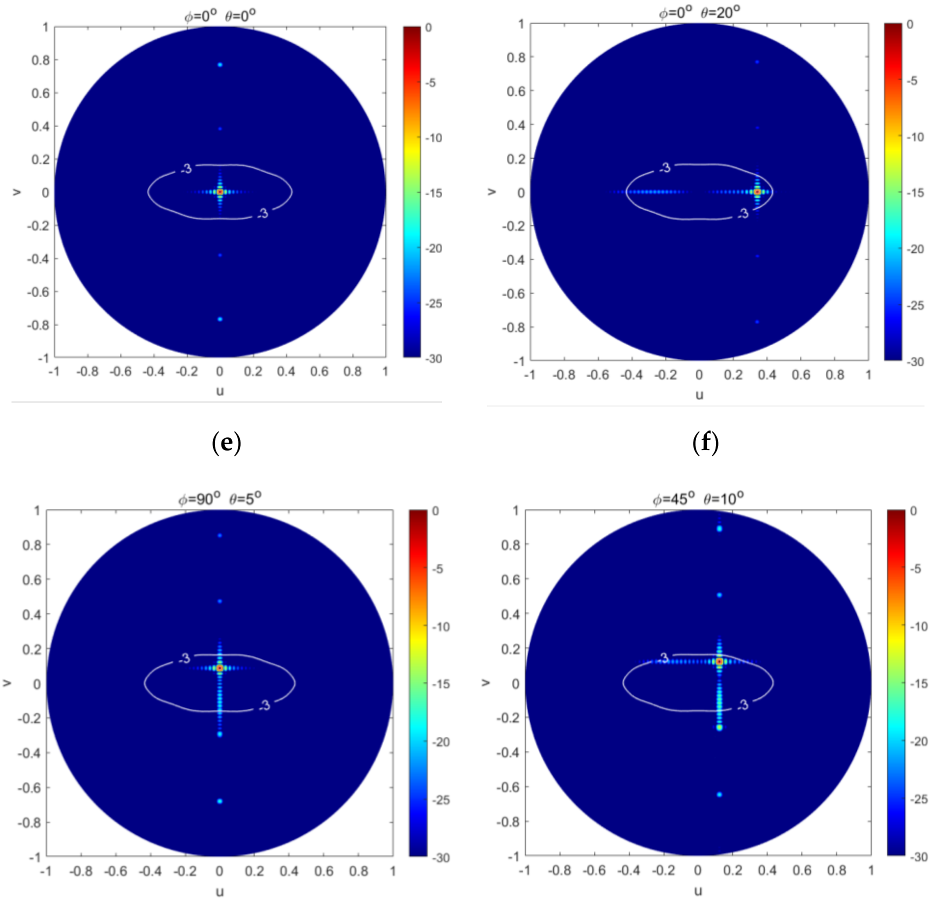

(**e**) (**f**)

(**g**) (**h**)

Figure 13. Array factor (**a**–**d**) and the radiation pattern (**e**–**h**) of the 65 × 19 array for various scan angles, where u = sinθcosφ and v = sinθsinφ. The −3 dB contour of the central sub-array radiation pattern of the 11 × 5 array is also shown.

4. Conclusions

In this work, we have proposed a novel antenna array architecture based on high-gain linear sub-arrays. An array structure has been designed so to achieve a directivity of 46.5 dBi, which is 2.2 dB higher than the corresponding 100% aperture efficiency limit. This performance has been obtained by exploiting the overlapping of multiple linear sub-arrays. The individual sub-array has a length of $2.653\lambda_0$ which might lead to the appearance of grating lobes while scanning. This non-ideality, however, has been properly taken into account during the design stage. As a matter of fact, the grating lobes are filtered by a proper shaping of the embedded element pattern of the sub-array. It has been, also, demonstrated that, for an accurate prediction of the array characteristics, it is key to properly model the edge effects. The inclusion of the edge effect limited the array scan range from ±9.3° to ±7.5° along the E-plane and from ±25.7° to ±24.2° along the H-plane, respectively. We have shown that the antenna array is intrinsically matched, though the relevant impedance matching band shifts with the scan angle. To mitigate this drawback, the integration of an external impedance matching network can be considered. The proposed design supports a single linear polarization. Although this might be sufficient in several operative scenarios, there are a large number of applications where simultaneous support of two polarizations is required. To achieve dual-polarization operation, suitable radiating elements have to be utilized. One example of such an element is the square dielectric-filled waveguide operating in TE_{01} and TE_{10} modes simultaneously. Another area for further improvement is the extension of the bandwidth of the proposed design. One way to achieve such an extension is to investigate alternative choices for the radiating elements. Another option, especially if a wide-band operation is required, is to use active non-foster loads as waveguides terminations [17,18]. By enabling dual polarization and broadband behavior, one can develop multibeam/multicolor arrays based on the proposed reactively loading approach. In this case, the coloring can be performed on the basis of polarization and frequency separation [19].

Some general properties and implementation schemes for linear and planar arrays organized in overlapped subarrays can be found in [20].

Author Contributions: Conceptualization, R.M., D.C., G.T., and A.B.S.; methodology, R.M., D.C., G.T., and A.B.S.; software, R.M.; supervision, D.C., G.T., and A.B.S.; validation, R.M., D.C., G.T., and A.B.S.; writing—original draft preparation, R.M.; writing—review and editing, R.M., D.C., G.T., and A.B.S. All authors have read and agreed to the published version of the manuscript.

Funding: This research received no external funding.

Acknowledgments: This study was conducted in the framework of a Network/Partnering Initiative between the European Space Agency, The Antenna Company, and the Eindhoven University of Technology, under the contract 4000114668/15/NL/MH.

Conflicts of Interest: The authors declare no conflict of interest.

References

1. Edstam, J.; Olsson, A.; Flodin, J.; Ohberg, M.; Henriksson, A.; Hansryd, J.; Ahlberg, J. *High-Capacity Microwave Is a Key Enabler for 5G*; Technical Report for Ericsson Microwave Outlook: Stockholm, Sweden, 2018.
2. Caratelli, D.; Toso, G.; Stukach, O.V.; Panokin, N.V. Deterministic Constrained Synthesis Technique for Conformal Aperiodic Linear Antenna Arrays—Part I: Theory. *IEEE Trans. Antennas Propag.* **2019**, *67*, 5951–5961. [CrossRef]
3. Caratelli, D.; Toso, G.; Stukach, O.V.; Panokin, N.V. Deterministic Constrained Synthesis Technique for Conformal Aperiodic Linear Antenna Arrays—Part II: Applications. *IEEE Trans. Antennas Propag.* **2019**, *67*, 5962–5973. [CrossRef]
4. Hong, W.; Jiang, Z.H.; Yu, C.; Zhou, J.; Chen, P.; Yu, Z.; Zhang, H.; Yang, B.; Pang, X.; Jiang, M.; et al. Multibeam Antenna Technologies for 5G Wireless Communications. *IEEE Trans. Antennas Propag.* **2017**, *65*, 6231–6249. [CrossRef]
5. Petrolati, D.; Angeletti, P.; Toso, G. A lossless beam-forming network for linear arrays based on overlapped sub-arrays. *IEEE Trans. Antennas Propag.* **2014**, *62*, 1769–1778. [CrossRef]
6. Maximidis, R.T.; Caratelli, D.; Toso, G.; Smolders, A.B. Design of Overlapped Subarrays Based on Aperture Reactive Loading. *IEEE Trans. Antennas Propag.* **2020**, *68*, 5322–5333. [CrossRef]
7. Angeletti, P.; Lisi, M. Multimode beamforming networks for space applications. *IEEE Antennas Propag. Mag.* **2014**, *56*, 62–78. [CrossRef]
8. Laue, H.E.A.; du Plessis, W.P. A Checkered Network for Implementing Arbitrary Overlapped Feed Networks. *IEEE Trans. Microw. Theory Tech.* **2019**, *67*, 4632–4640. [CrossRef]
9. Caille, G.; Chiniard, R.; Thevenot, M.; Chreim, H.; Arnaud, E.; Monediere, T.; De Maagt, P.; Palacin, B. Electro-magnetic band-gap feed overlapping apertures for multi-beam antennas on communication satellites. In Proceedings of the 8th European Conference on Antennas and Propagation (EuCAP 2014), The Hague, The Netherlands, 6–11 April 2014.
10. Llombart, N.; Neto, A.; Gerini, G.; Bonnedal, M.; De Maagt, P. Leaky wave enhanced feed arrays for the improvement of the edge of coverage gain in multibeam reflector antennas. *IEEE Trans. Antennas Propag.* **2008**, *56*, 1280–1291. [CrossRef]
11. Blanco, D.; Rajo-Iglesias, E.; Montesano Benito, A.; Llombart, N. Leaky-Wave Thinned Phased Array in PCB Technology for Telecommunication Applications. *IEEE Trans. Antennas Propag.* **2016**, *64*, 4288–4296. [CrossRef]
12. Smolders, A.B.; Dubok, A.; Tessema, N.M.; Chen, Z.; Al Rawi, A.; Johannsen, U.; Bressner, T.; Milosevic, D.; Gao, H.; Tangdiongga, E.; et al. Building 5G Millimeter-Wave Wireless Infrastructure: Wide-Scan Focal-Plane Arrays With Broadband Optical Beamforming. *IEEE Antennas Propag. Mag.* **2019**, *61*, 53–62. [CrossRef]
13. Mathworks Matlab. 2017. Available online: www.matlab.com (accessed on 5 July 2017).

14. Dassault Systems CST. 2019. Available online: https://www.cst.com/2019 (accessed on 10 June 2019).
15. Ugray, Z.; Lasdon, L.; Plummer, J.; Glover, F.; Kelly, J.; Marti, R. Scatter Search and Local NLP Solvers: A Multistart Framework for Global Optimization. *INFORMS J. Comput.* **2007**, *19*, 328–340. [CrossRef]
16. Mailloux, R.J. *Phased Array Antenna Handbook*; Artech House Antennas and Propagation Library: Boston, MA, USA, 2005; ISBN 9781580536899.
17. Jacob, M.M.; Long, J.; Sievenpiper, D.F. Non-foster loaded parasitic array for broadband steerable patterns. *IEEE Trans. Antennas Propag.* **2014**, *62*, 6081–6090. [CrossRef]
18. Batel, L.; Rudant, L.; Pintos, J.F.; Clemente, A.; Delaveaud, C.; Mahdjoubi, K. High directive compact antenna with non-foster elements. In Proceedings of the 2015 International Workshop on Antenna Technology (iWAT), Seoul, Korea, 4–6 March 2015.
19. Toso, G. The beauty of multibeam Antennas. In Proceedings of the 2015 9th European Conference on Antennas and Propagation (EuCAP), Lisbon, Portugal, 13–17 April 2015.
20. Angeletti, P.; Toso, G.; Petrolati, D. Beam-Forming Network for an Array Antenna and Array Antenna Comprising the Same. U.S. Patent 9,374,145, 26 November 2012.